RESEARCH ARTICLE

NANO · MICRO small
www.small-journal.com

Elucidating Phase Transformation and Surface Amorphization of $Li_7La_3Zr_2O_{12}$ by In Situ Heating TEM

*Hongkui Zheng, Mingjie Xu, and Kai He**

Garnet-type $Li_7La_3Zr_2O_{12}$ (LLZO) solid-state electrolytes hold great promise for the next-generation all-solid-state batteries. An in-depth understanding of the phase transformation during synthetic processes is required for better control of the crystallinity and improvement of the ionic conductivity of LLZO. Herein, the phase transformation pathways and the associated surface amorphization are comparatively investigated during the sol–gel and solid-state syntheses of LLZO using in situ heating transmission electron microscopy (TEM). The combined ex situ X-ray diffraction and in situ TEM techniques are used to reveal two distinct phase transformation pathways (precursors → $La_2Zr_2O_7$ → LLZO and precursors → LLZO) and the subsequent layer-by-layer crystal growth of LLZO on the atomic scale. It is also demonstrated that the surface amorphization surrounding the LLZO crystals is sensitive to the postsynthesis cooling rate and significantly affects the ionic conductivity of pelletized LLZO. This work brings up a critical but often overlooked issue that may greatly exacerbate the Li-ion conductivity by undesired synthetic conditions, which can be leveraged to ameliorate the overall crystallinity to improve the electrochemical performance of LLZO. These findings also shed light on the significance of optimizing surface structure to ensure superior performance of Li-ion conductors.

1. Introduction

Lithium-ion batteries (LIBs) are essential components of modern society, particularly for applications in electronic devices, electric transportation, and power grids.[1,2] To address the safety concerns related to electrolyte flammability, Li dendrite formation, and unstable solid electrolyte interphase (SEI) in traditional LIBs,[3] solid-state batteries (SSBs) are being developed as a potential solution for the next-generation, high-performance, and safe energy storage technology.[4–6] Garnet-type $Li_7La_3Zr_2O_{12}$ (LLZO) solid-state electrolytes (SSEs) are one of the most promising candidates due to their relatively high ionic conductivity (up to 1 mS cm^{-1}),[7,8] wide electrochemical window,[9] and excellent stability against Li metal.[10] Crystalline LLZO may exist in cubic or tetragonal phase.[11,12] The cubic LLZO with disordered Li arrangement and shorter Li—Li atomic distance is preferably desired because its ionic conductivity is typically two orders of magnitude higher than that of the tetragonal LLZO.[3,13] In contrast, amorphous LLZO is a poor Li-ion conductor, with 2–3 orders of magnitude lower ionic conductivity compared to the cubic polymorph.[14,15] Such a large variation in LLZO's ionic conductivity is caused by the differences in their crystal structure and crystallinity. This requires good control of the desired LLZO structures by compositional engineering and synthetic optimization. Nevertheless, despite the majority of previous efforts in improving the Li-ion conductivity by stabilizing the formation of cubic LLZO phase through various cation substitutions (e.g., Al^{3+}, Ga^{3+}, and Ta^{5+}),[7,8,16] significantly less attention has been paid to mitigating the negative impact of the surface amorphization of crystalline cubic LLZO. From this perspective, we are motivated to address this critical issue by fundamentally understanding the mechanism of LLZO amorphization and its relationship with phase transitions during synthesis processes. Solid-state and sol–gel syntheses are the two most common methods used to obtain LLZO powders on a large scale, but their specific synthetic parameters are different, and they may cause variations in purity, phase composition, crystal structure, morphology, and grain size of the resulting materials, consequently affecting the SSE's electrochemical performance. Conventional solid-state synthesis typically requires longer calcination times and higher temperatures than the sol–gel method for the synthesis of LLZO,[17] implying that the corresponding phase transformation pathways are different and that the crystallinity of intermediate and final phases may also differ.[18–21] It is thus necessarily important to clarify the exact phase transformations and the associated crystal structure and crystallinity changes over the entire synthesis process.

H. Zheng, K. He
Department of Materials Science and Engineering
University of California
Irvine, CA 92697, USA
E-mail: kai.he@uci.edu

M. Xu
Irvine Materials Research Institute
University of California
Irvine, CA 92697, USA

The ORCID identification number(s) for the author(s) of this article can be found under https://doi.org/10.1002/smll.202304799

DOI: 10.1002/smll.202304799

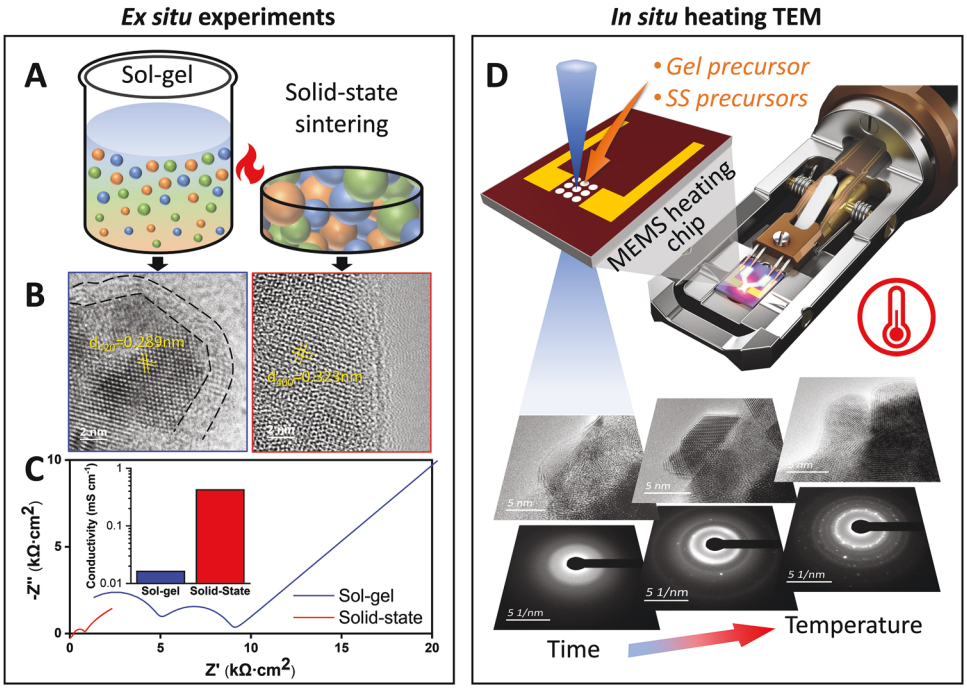

Figure 1. Design of ex situ and in situ experiments for determination of phase transformations during LLZO synthesis. A) Schematic illustration of LLZO synthesis through sol–gel and solid-state (SS) sintering methods. B) HRTEM images of sol–gel and solid-state synthesized LLZO with the dashed lines showing an amorphous layer on the surface of sol–gel synthesized LLZO nanoparticles. C) Nyquist impedance of sol–gel and solid-state synthesized LLZO pellets with the inset showing the corresponding ionic conductivity values. D) MEMS-based in situ heating TEM setup for real-time observation of LLZO calcination of gel or SS precursors by direct imaging and electron diffraction at various temperatures.

Previously, researchers have employed X-ray diffraction (XRD) to track the phase transitions by postmortem measurements of the phase composition at a series of temperatures,[21] which, however, cannot effectively capture the formation of amorphous phase during the synthesis. Transmission electron microscopy (TEM) has also been widely used to study phase transitions by providing the overall phase determination by electron diffraction along with the local crystal lattice information by high-resolution imaging on the atomic scale.[22,23] Particularly, the recent advancement of in situ TEM further offers new capability to carry out such phase, structural, and morphological characterizations in real time and at the relevant length scales from the same sample,[24–26] manifesting itself as a powerful tool for the purpose mentioned above.

In this work, we designed a comparative investigation to study the similarity and differences in the phase transformation, structure evolution, and surface amorphous formation during the synthesis of LLZO via both sol–gel and solid-state methods using in situ heating TEM combined with ex situ XRD. Two distinct phase transformation pathways were observed, including the two-step transition from the pristine precursors to $La_2Zr_2O_7$ (LZO) and then to LLZO and the direct transition from precursors to LLZO. The former pathway was found to govern the sol–gel synthesis while both pathways could concurrently occur in the solid-state synthesis. The subsequent layer-by-layer growth of single-crystal LLZO along the [422] orientation was determined by in situ high-resolution TEM (HRTEM). The formation of the anomalous amorphous layer surrounding LLZO crystals was in situ observed during the postsynthesis cooling stage, which was further analyzed quantitatively as a function of the cooling rate. We believe that addressing this critical but often overlooked issue in LLZO synthesis is of great importance for improving the ionic conductivity and electrochemical performance of Li-ion conductors.

2. Results and Discussion

2.1. Experimental Design

Figure 1 shows the schematic illustration of our experimental design and setup of the sol–gel synthesis and solid-state sintering of LLZO samples as well as the following test of electrochemical properties and TEM characterization through both ex situ and in situ experimentations. We first synthesized LLZO materials using both the sol–gel method and the solid-state sintering (Figure 1A; for details see the "Experimental Section") and then characterized the as-synthesized LLZO particles using HRTEM (Figure 1B). It is found that the sol–gel synthesis produces a much smaller particle size (≈5 nm) than that of the solid-state method (>2 μm; see Figure S1 in the Supporting Information) and meanwhile that a much thicker (≈2 nm) amorphous layer (labeled by the dashed lines) ubiquitously forms on the surface of crystalline cubic LLZO nanoparticles in contrast to the barely visible amorphous layer for solid-state sintered LLZO. This indicates that a significant amount of surface amorphization was induced during the calcination of gel powders, which is very likely to cause large resistance when sintered into LLZO pellets. To verify this speculation, we pelletized the LLZO powders made from both

syntheses into LLZO pellets and measured their resistance using the electrochemical impedance spectroscopy (EIS) technique, which was further used to obtain the ionic conductivity of the prepared LLZO pellets, as shown in Figure 1C. The Nyquist plot indicates the enormously high bulk resistance for sol–gel synthesized LLZO compared to that of the solid-state sintered LLZO. Consequently, the measured ionic conductivity of sol–gel LLZO (0.016 mS cm^{-1}) is more than one order of magnitude lower than the ionic conductivity of LLZO made by the solid-state method (0.422 mS cm^{-1}), as shown in Figure 1C (inset) and Figure S2 (Supporting Information). Given all the same parameters for pelletization and EIS measurements, the formation of additional amorphous layers should be accountable for the poor ionic conductivity,[14,15] confirming our hypothetical thinking that the crystallinity (or surface amorphization) of as-synthesized LLZO materials plays a critical role to influence ionic conductivity to the extent that was greatly underestimated, especially for sol–gel LLZO powders with small primary particle size.

To further elucidate how such amorphous layers are formed during different synthetic routes and how they are related to the phase transformation pathways, we intended to carry out in situ heating TEM experiments to investigate the phase transformation processes during sol–gel and solid-state syntheses (Figure 1D). Specifically, we use an in situ heating holder based on the micro-electromechanical system (MEMS) technology to ensure minimal thermal drift for reliable HRTEM imaging along with precision temperature control and tunable temperature ramp rates. The prepared gel precursors or solid-state precursors can be directly dispersed onto the MEMS heating chip and then heated up to the desired temperatures ranging from room temperature (RT) up to 950 °C to reproduce the calcination process inside the TEM. Real-time TEM imaging and electron diffraction can be captured as a function of temperature to provide information about phase transformations in real space and reciprocal space (details can be found in the "Experimental Section").

2.2. Phase Transformation Revealed by Ex Situ XRD

We first examined the phase transformation during LLZO synthesis through sol–gel and solid-state routes using ex situ XRD at various calcination temperatures (**Figure 2**). Figure 2A,B shows the XRD patterns acquired during the sol–gel synthesis and the corresponding phase compositions as a function of temperature. The initially dried xerogel precursor exhibited an amorphous nature without any prominent peak, representing the amorphous metal–organic complex.[21] These xerogel powders were calcinated at elevated temperatures up to 900 °C. The broad peaks appeared in the temperature range from 400 to 600 °C, indicating the decomposition of the metal–organic complex to form precursor mixtures composed of lithium carbonate (Li_2CO_3), lanthanum oxide (La_2O_3), and zirconium oxide (ZrO_2) (standard JCPDF information in Figure S3 and Table S1 in the Supporting Information). The Rietveld refinement was conducted to quantitatively analyze the mass fraction of each phase component at different temperatures (Figures S4 and S5, Supporting Information). Strong LZO diffraction peaks started to appear at 650 °C, indicating that the gel precursors were entirely transformed into LZO, which was continuously transformed into LLZO when the temperature was increased to 700—750 °C. It is noted that some minor reaction byproducts containing $Li_{0.52}La_2(CO_3)_{0.74}O_{2.26}$ (lithium-containing phase of $La_2O_2CO_3$)[27] and excess La_2O_3 were also found in the same temperature range, consistent with previous reports.[18] With the further increase of calcination temperature to 800 °C, LZO was mostly transformed into the cubic LLZO without forming any tetragonal-LLZO impurities, since Ta-doping was added when preparing xerogel to stabilize the cubic-LLZO phase. The content of the LLZO phase was gradually increased upon continued temperature increase and finally completed at 900 °C with high purity. Additional heating to a higher temperature may cause Li loss and decomposition of LLZO into LZO, which is undesired and often avoided. As a comparison, the calcination of solid-state precursors was also carried out under the same condition and in the same temperature range. Figure 2C,D shows the XRD patterns acquired during the solid-state synthesis and the corresponding phase compositions as a function of temperature. The RT XRD pattern indicates the precursors including Li_2CO_3, La_2O_3, ZrO_2, and tantalum oxide (Ta_2O_5). These diffraction peaks remained in the mixture when the temperature was below 700 °C. When heating to temperatures between 500 and 700 °C, intermediate byproducts, including $Li_{0.52}La_2(CO_3)_{0.74}O_{2.26}$ and $LiTaO_3$, started to appear and then diminish. Then, the LZO phase started to appear from 600 °C and gradually increased to the peak content at 700 °C, and then nearly vanished at 750 °C. This process is associated with the phase transformation from LZO to LLZO occurred at 750 °C, which is similar to the LZO to LLZO transition in sol–gel synthesis. Despite this similarity, we also found a peculiarity for the solid-state synthesis that the LZO phase appears as a minor admixture (30%) to the rest majority of precursors at 700 °C and the latter reagents can directly transform into the LLZO phase at 750 °C without necessarily passing through the LZO phase. It is implied that two distinct phase transition pathways may concurrently take place in the solid-state reactions: 1) precursors → LZO→ LLZO, and 2) precursors → LLZO. With further increase of temperature from 800 to 900 °C, the LLZO phase continued to increase its content and purity. It is noted that a very slight amount (<1%) of LZO reappears at 900 °C due to the decomposition of LLZO into LZO and Li_2O, which causes Li loss and is unwanted, suggesting that LLZO sintering should not exceed 900 °C. Comparing the phase transformations for sol–gel and solid-state syntheses side by side, although a similar precursor → LZO → LLZO phase transition pathway exists in both scenarios, the corresponding transition temperatures are slightly different. This is because the sol–gel method provides homogeneous mixing of precursors at the molecular level, which facilitates the phase transition from the gel precursor to LZO to occur homogeneously and concurrently within the entire sample, leading to a transition pathway close to the thermodynamic route followed by the LZO → LLZO transformation. In contrast, the mixing of reaction agents in solid-state precursors is less homogeneous, which slows down the reaction speed of the precursors → LZO transformation and postpones its completion. The phenomenon of bypassing the 100% LZO formation in solid-state synthesis may not be simply attributed to the inhomogeneity induced overlap between reactions of precursors → LZO and LZO → LLZO, but instead, it is also related to the kinetics of the phase transformations, which override the delayed precursors → LZO

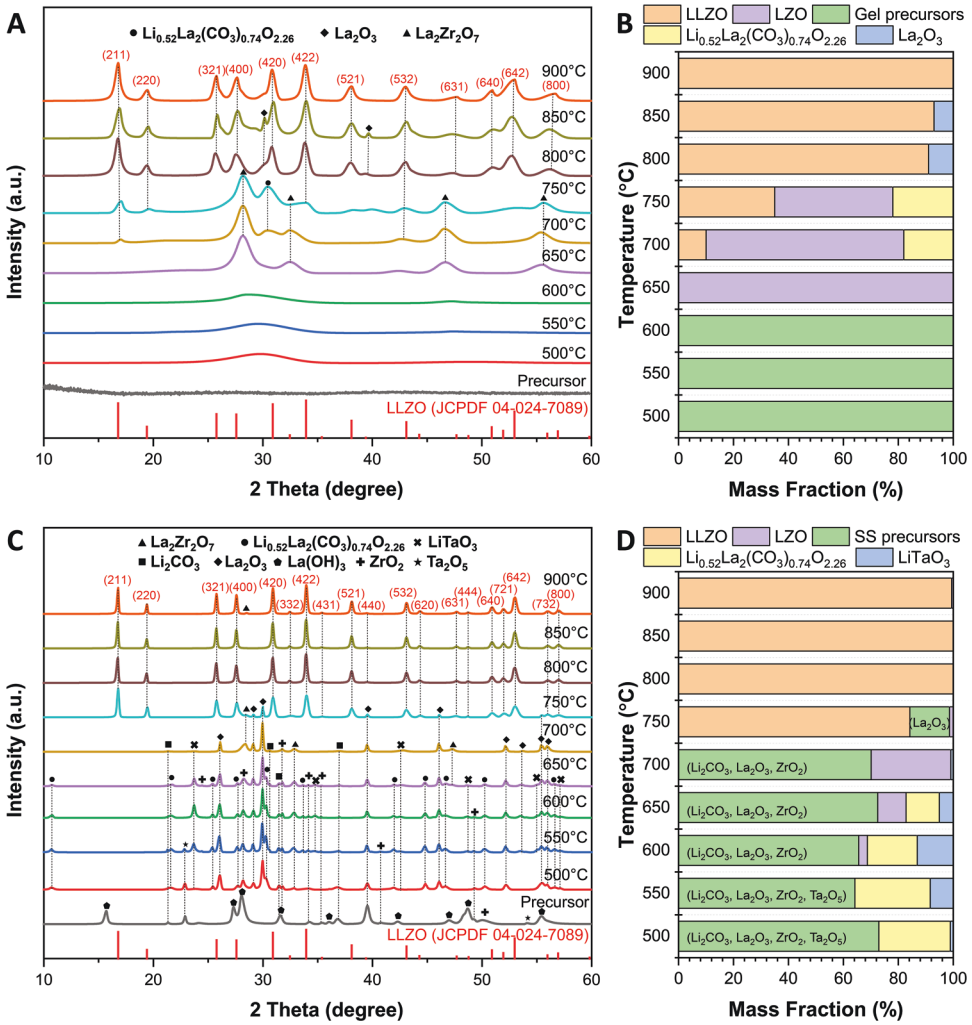

Figure 2. Phase transformations during sol–gel and solid-state syntheses revealed by ex situ XRD. A) XRD patterns and B) the corresponding phase compositions at different temperatures during the sol–gel synthesis. C) XRD patterns and D) the corresponding phase compositions at different temperatures during the solid-state synthesis. The Rietveld refinement of raw data can be found in Figures S4 and S5 (Supporting Information).

reaction when the temperature rises sufficiently high to trigger the direct precursors → LLZO reaction. It is also worth noting that the solid-state method can lead to much larger particle size and better crystallinity (manifested by the sharper XRD peaks) compared to the sol–gel method. The phase transformations revealed by XRD confirmed the phase transition temperature for cubic LLZO, which was regarded as guidelines for the following in situ heating TEM experiments.

2.3. In Situ Heating TEM for Sol–Gel Synthesis

Although XRD can reveal the phase transformation, it is unable to effectively probe the amorphous phase. Thus, we performed in situ heating TEM that allows phase transformation to be identified by combined imaging and diffraction techniques. Based on the XRD results, we determined the heating schedule for the calcination of the sol–gel sample at the temperature from RT to 950 °C and maintained for 1 h at each temperature, as shown in **Figure 3**A. Figure 3B shows a series of enlarged HRTEM images (original images shown in Figure S6 in the Supporting Information) taken at the designated temperatures along with the corresponding fast Fourier transform (FFT) from the entire 100 nm × 100 nm region of the original images. The morphology of the pristine xerogel sample experienced a slight change, mainly observed as the lateral expansion, upon heating to high temperatures. Although crystalline phases are visible in Figure 3B (1–5), it is ambiguous to identify the crystallization process solely by direct imaging from a coexisted amorphous–crystalline mixture; thus, we use the FFT pattern to track the underlying phase transformations. For this specific region of interest, FFT patterns display amorphous characteristics from RT to 650 °C (Figure 3B (1–4)) and then show the appearance of crystalline LZO phase at 750 °C (Figure 3B (5–6)). Later, the transformation to the crystalline cubic-LLZO phase occurred at 900 °C, and its crystallinity was increased at 950 °C, as evidenced by more visible crystalline reflections in the FFT (Figure 3B (7–8)). The initial amorphous gel was mostly transformed into crystalline

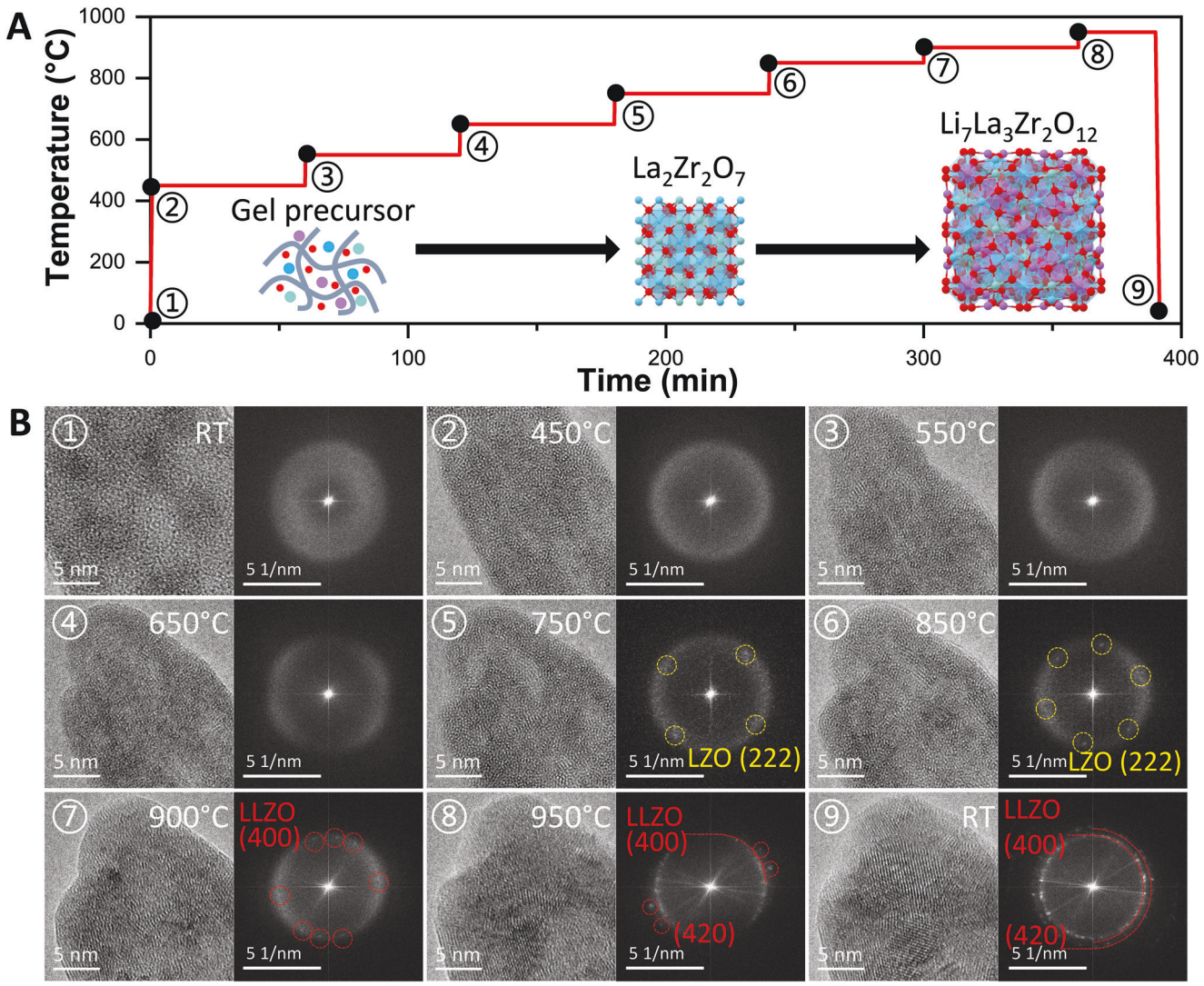

Figure 3. In situ heating experiments for the sol–gel synthesis of LLZO. A) Temperature profile used for in situ heating TEM. B) HRTEM images and the corresponding fast Fourier transform (FFT) patterns from 1–9) the entire region of interest as a function of temperature during in situ heating.

LLZO after calcinating at 950 °C and the subsequent cooling to RT (Figure 3B (9)), while a small portion of unreacted amorphous may present likely due to insufficient calcination time compared to the real-world sol–gel synthesis. The in situ heating TEM revealed the same precursors → LZO→ LLZO transition pathway as that identified by XRD above.

Since the interested phase transformations occurred from 750 to 950 °C, we also conducted in situ electron diffraction as a function of temperature from a much larger area of the xerogel sample to identify crystalline phase evolution in this temperature range, as shown in **Figure 4**A. The diffraction pattern of xerogel at RT exhibits amorphous rings, consistent with the XRD and FFT results. The first diffraction spot appeared after heating at 750 °C for 30 min, identified as the (440) plane of the LZO phase. After another 30 min holding at 750 °C, the content of the LZO phase became predominant (more diffraction spots) while the cubic-LLZO phase was also formed, as identified by its diffraction spot from the (800) plane. Starting from the temperature increased to 850 °C, more diffraction spots from LLZO emerged, and LZO reflections became less and relatively weaker at 900 °C. After heating at 950 °C, the final product was almost fully transformed into polycrystalline LLZO with distinct diffractions from (400), (420), (521), (640), and (800) planes. During the course of the in situ electron diffraction experiments, we also acquired a series of HRTEM images from a specific region of interest to highlight the crystal lattice evolution during the growth of an LLZO single crystal, as shown in Figure 4B. It is found that the LLZO single crystal was first formed at 750 °C with the {422} terminating facets (d_{422} = 2.63 Å) and later continued to grow layer by layer along the [422] orientation into a larger crystal with a well-defined lattice structure, and no amorphous at the temperature up to 950 °C. However, it is surprisingly noted that the surface of LLZO single crystals transformed from a sharp crystalline structure to an amorphous state when the sample was cooled down to RT at a cooling rate of 10 °C s^{-1}. This intriguing phenomenon of the formation of ≈2 nm surface amorphous layer is consistent with

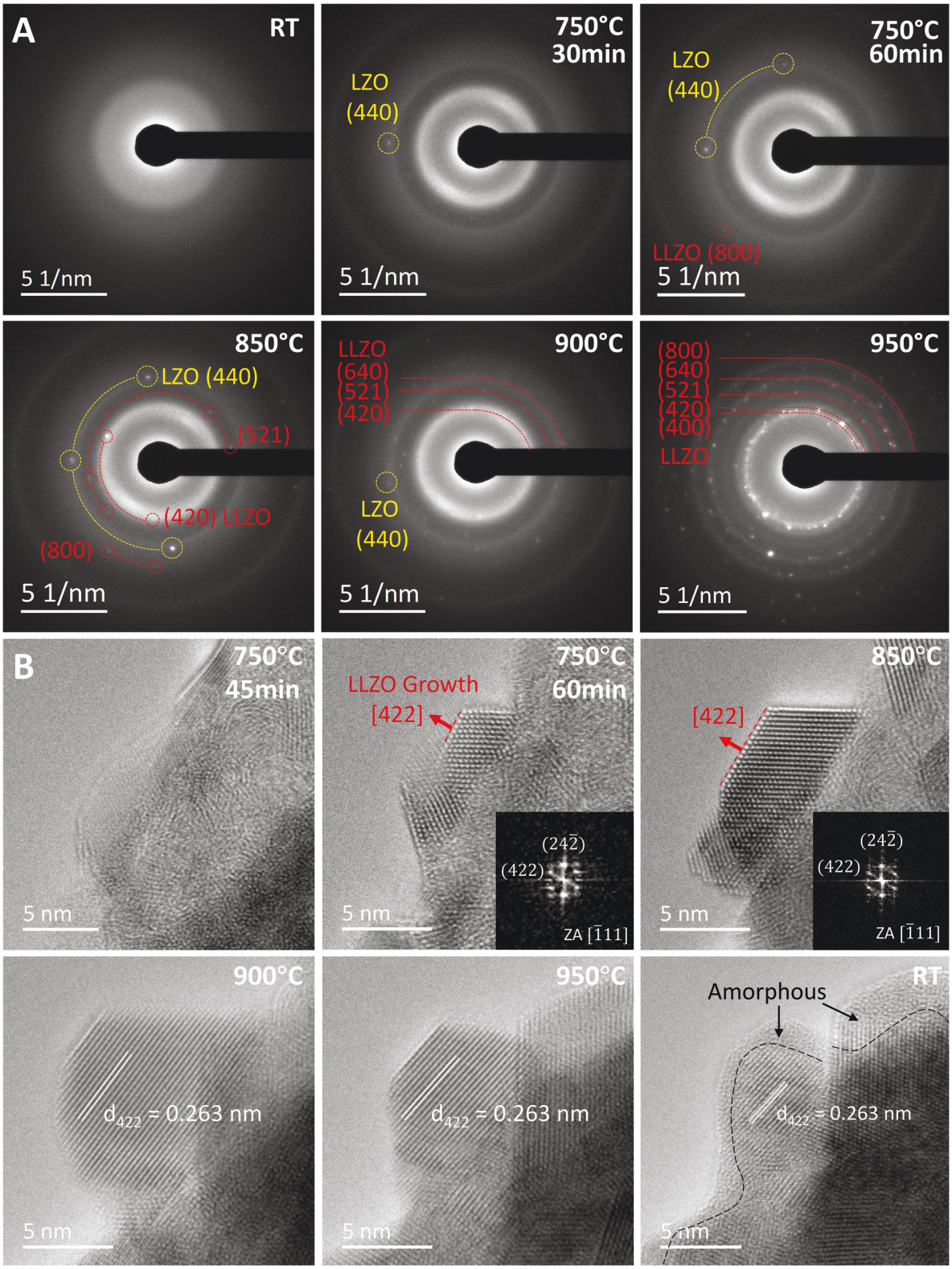

Figure 4. In situ electron diffraction and HRETM imaging during sol–gel synthesis of LLZO. A) In situ electron diffraction patterns and B) in situ HRTEM images, as a function of temperature during the sol–gel synthesis. The intermediate phases are labeled in the diffraction pattern. The crystal lattices and the corresponding FFT insets illustrate the layer-by-layer pathway of LLZO crystal growth.

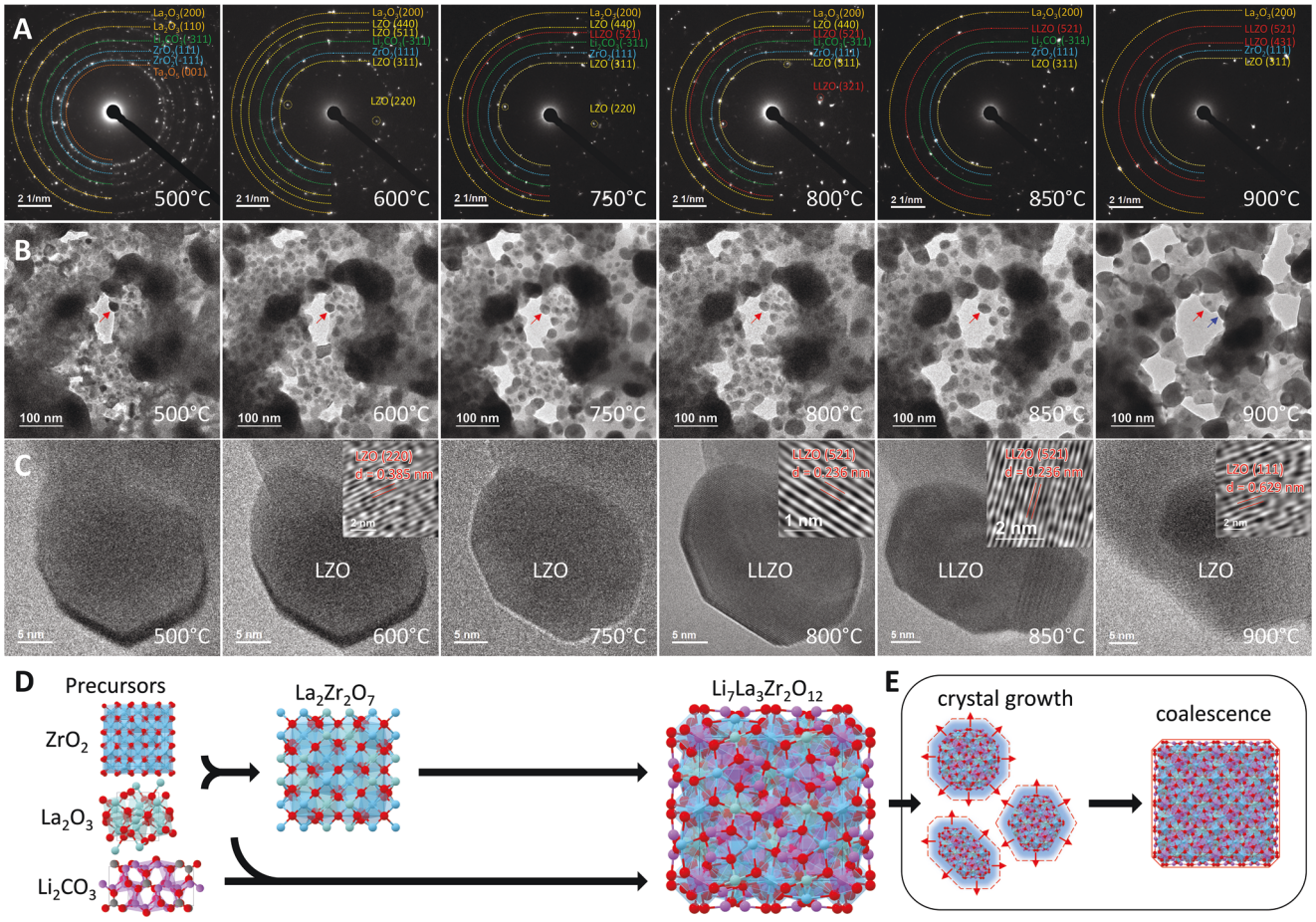

Figure 5. In situ electron diffraction and HRETM imaging during solid-state synthesis of LLZO. A) Temperature-dependent electron diffraction patterns. B) TEM images of a large area. C) HRTEM images of an individual particle (marked by red arrows in panel (B)), captured during the solid-state synthesis showing the LLZO formation process upon heating. Schematic illustration showing D) phase transitions via precursors → LZO → LLZO and precursors → LLZO pathways. E) The subsequent crystal growth and coalescence processes to form large LLZO particles.

the observation in the ex situ synthesized product (Figure 1B). Such an undesired crystalline-to-amorphous transformation may be due to the rapid cooling of crystalline materials, which needs further investigation to clarify, but meanwhile should bring up more caution to avoid it for the practical manufacturing of LLZO solid electrolytes.[28,29]

2.4. In Situ Heating TEM for Solid-State Synthesis

In order to reveal the phase transformation pathways during the solid-state synthesis and elucidate the mechanism of the surface amorphization, we also carried out the comparative in situ heating TEM experiments for the solid-state sintering of LLZO. **Figure 5**A–C shows the temperature-dependent electron diffraction patterns and the corresponding TEM images taken during LLZO sintering from 500 to 900 °C. All solid-state precursors containing Li_2CO_3, La_2O_3, ZrO_2, and Ta_2O_5 were identified by electron diffraction, which were also visualized as enormous fine nanoparticles in the TEM image at 500 °C. As the temperature increased to 600 °C, the phase transition to LZO started to occur making the fine precursor nanoparticles transformed into larger particles with less quantity. It is also confirmed by the enlarged HRTEM image of an individual particle (marked by the red arrow in Figure 5B), in which the lattice fringes of LZO (220) crystal planes were clearly visible. Then, the transition to LLZO phase was found at 750 °C and continued to proceed as the temperature was increased to 900 °C. The HRTEM image taken at 800 °C in Figure 5C (enlarged raw images in Figure S7 in the Supporting Information) indicates the single-crystal LZO particle was transformed into the LLZO phase, evident by the LLZO (521) lattice fringes. It is noted that the precursors, LZO and LLZO, coexisted during this process, which is consistent with the ex situ XRD results shown in Figure 2D, suggesting two possible phase transition pathways via precursors → LZO → LLZO and precursors → LLZO, respectively, as illustrated in the schematics in Figure 5D. The LLZO single-crystalline particle continued to grow and slightly changed its shape when the temperature was increased to 850 °C. Nevertheless, nearly no amorphous was found in solid-state-sintered LLZO single crystals. (It should be noted that the dark fringes in this image are not crystal defects but stead the Moiré fringes arising from the interference with another overlapped crystalline particle underneath.) However, at 900 °C, this LLZO particle disappeared, leaving behind an

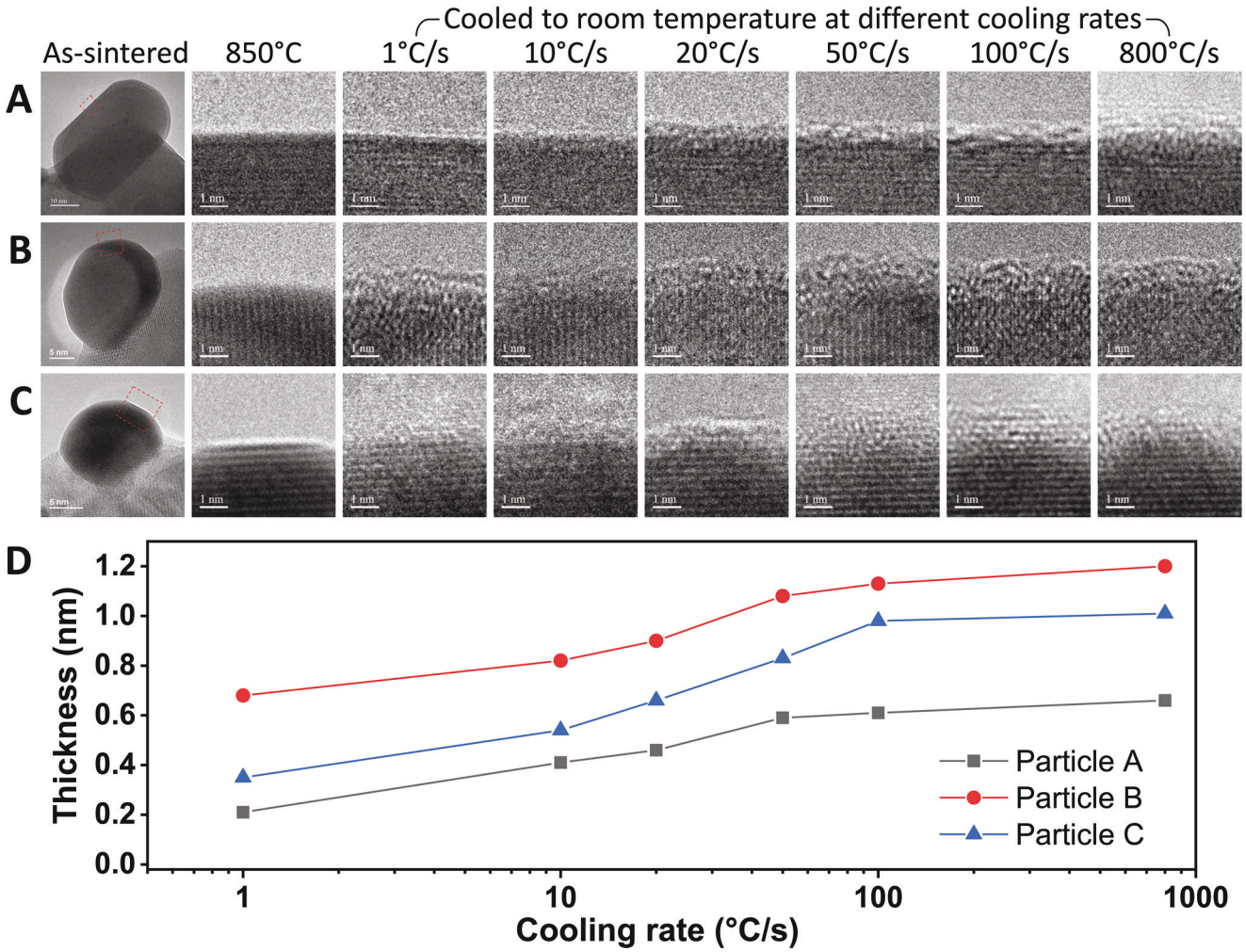

Figure 6. The effect of postsynthesis cooling rate on the crystallinity of solid-state sintered LLZO. A–C) Three series of HRTEM images of LLZO single crystals and their enlarged surface regions at the as-sintered state and after cooling to RT at various cooling rates (1–800 °C s^{-1}). D) The accumulated thickness of the surface amorphous layer on LLZO single crystals as a function of cooling rate.

unreacted LZO particle (the dark contrast area is likely to be a partially formed LLZO, but we did not resolve its lattice fringes because it was not aligned to any close zone axis). We also found that a few other particles in the close vicinity vanished as well, implying that these particles were likely coalesced into a larger LLZO crystal marked by the blue arrow in Figure 5B (900 °C), also shown in Figure S7 (Supporting Information). Based on these observations, we propose a plausible crystal growth and coalescence model shown in Figure 5E.

To clarify how the surface amorphization occurred during the cooling stage, we further examined the impact of the cooling rate (from 1 to 800 °C s^{-1}) on the thickness of the amorphous layer formed on the surface of LLZO. **Figure 6**A–C shows the morphology evolution of three exemplary LLZO single crystals produced by the solid-state synthesis, and the enlarged HRTEM of their surfaces (marked by red dashed boxes) in the as-sintered conditions at 850 °C and after multiple cooling cycles to RT at various cooling rates. The morphologies of these LLZO single crystals did not change throughout the repeated heating and cooling cycles, but the accumulated thickness of the surface amorphous layer was found to be closely related to the cooling rate. The quantitative measurement of the thickness of surface amorphous layers is shown in Figure 6D, which indicates that surface amorphization is monotonically increased with an increase of the cooling rate. The dependence of amorphous thickness and cooling rate are in a consistent trend for all three particles, suggesting that a slow cooling rate (such as <10 °C s^{-1}) is preferable to obtain minimal surface amorphization, while when the cooling rate is greater than 100 °C s^{-1}, the thickness of the surface amorphous layer is saturated. The root cause of this intriguing phenomenon requires in-depth investigation. Based on our observations in this study, we may infer that the surface of a crystalline LLZO particle is of less crystallinity and stability than its interior. This is because that the LLZO particle prefers the layer-by-layer growth (Figure 4) and that the LLZO tends to decompose at a high temperature (Figure 2D); both are surface-related processes that make the surface atoms not so perfectly coherent to the underneath LLZO crystal lattice. In this scenario, an abrupt temperature change may disrupt the crystal lattice and lead to surface amorphization in the manner faster and severer than the slow cooling down. It is

also suggested that atomistic simulations may provide additional insights from the theoretical perspective. Compared to the surface amorphous layer formed in sol–gel synthesis, the solid-state sintering induces much less amorphization. Furthermore, when taking the crystal size into consideration, the relative amount of surface amorphous per volume is significantly less than that of the sol–gel synthesis, which is responsible for the much higher overall crystallinity of solid-state-sintered LLZO, demonstrating that the solid-state sintering is a preferable synthetic strategy to produce LLZO with the improved ionic conductivity. From the information obtained in this study, it is suggested to control the cooling rate at or below ≈1 °C s^{-1} to optimize the crystallinity of the synthesized LLZO. For conventional furnace sintering, this level of slow cooling has been generally adopted as a common practice; however, for the emergence of new approaches using ultrafast sintering[30–33] and quenching[34,35] to tune the microstructure, compositional segregation, and ionic conductivity of solid electrolytes, the effect of cooling rate on surface amorphization might be overlooked. From this perspective, this work provides useful benchmarks to guide the optimization of ultrafast heating and cooling processes, especially when the cooling plays a mixed role and a compromise must be made accordingly.

3. Conclusion

In summary, this study revealed the phase transformations during sol–gel and solid-state syntheses of LLZO solid electrolytes and elucidated the effect of postsynthesis cooling rate on the formation of surface amorphous layer for single-crystalline LLZO using combined in situ TEM and ex situ XRD characterization techniques at different length scales. Distinct phase transformation pathways were identified for both sol–gel and solid-state synthetic methods. The sol–gel synthesis primarily proceeds through the precursors → LZO → LLZO pathway, while both the two-step precursors → LZO → LLZO and the direct precursors → LLZO pathways concurrently occur in solid-state synthesis. Atomic-scale investigation showed that Li diffusion into the LZO lattice to transform the structure into LLZO started at 750 °C and the subsequent LLZO crystal growth followed a layer-by-layer growth pathway along the [422] orientation. It is found that an amorphous layer surrounding LLZO crystals was commonly formed in sol–gel and solid-state syntheses, although the overall decrease of crystallinity is significantly less in solid-state sintered LLZO crystals. The postsynthesis cooling rate was found to be one of the essential factors affecting the thickness of surface amorphization, which suggested that keeping the cooling rate at or below 1 °C s^{-1} can effectively ameliorate the overall crystallinity of LLZO. This work provides fundamental insights for optimizing the synthesis of ceramic solid electrolyte materials and particularly offers implications for real-world production to pay special attention to avoiding unwanted surface amorphization and enhancing the crystallinity for improved electrochemical performance.

4. Experimental Section

Materials: Lithium carbonate, lanthanum oxide, lanthanum hydroxide ($La(OH)_3$), zirconium oxide, reagent alcohol, isopropyl alcohol, and nitric acid were purchased from Fisher Scientific. Tantalum oxide and zirconium ethoxide ($Zr(OC_2H_5)_4$) were obtained from Alfa Aesar. Tantalum chloride ($TaCl_5$) was purchased from TCI Chemicals and citric acid was acquired from Ward's Science.

Sample Preparation: The sol–gel synthesis was performed following the Pechini sol–gel method,[36] in which Li_2CO_3 and La_2O_3 precursors were initially dissolved in dilute nitric acid, and then $Zr(OC_2H_5)_4$ and $TaCl_5$ were dissolved in alcohol upon heating and stirring. Here, the addition of Ta^{5+} was only for the purpose of stabilizing the formation of the cubic-LLZO phase. The molar ratio of Li, La, Zr, and Ta was defined as 6.4:3:1.4:0.6 in this work. The two solutions were then mixed with the addition of citric acid as the chelating agent. After heating at 120 °C for 8 h and drying at 200 °C for 24 h to burn out the unwanted organics, yellow xerogel was obtained and ground for the next-step calcination or in situ heating TEM experiment. The dried gel was calcined from 500 to 900 °C at intervals of 50 °C for 2 h at a heating rate of 3 °C min^{-1} in the Ar atmosphere followed by 3 °C min^{-1} cooling to room temperature in a tube furnace to produce multiple samples at different temperatures for XRD analysis of the phase transformation during the sol–gel synthesis. For the solid-state synthesis, Li_2CO_3, La_2O_3 (containing partial $La(OH)_3$), ZrO_2, and Ta_2O_5 precursors were added in the same molar ratio as mentioned above and mixed using a planetary ball mill in isopropyl alcohol solvent at 500 rpm for 18 h. After drying, the precursor powders were heated to the same series of temperatures (500–900 °C, 50 °C interval) using the same temperature ramp rate (3 °C min^{-1} for heating and cooling) as the sol–gel synthesis in Ar atmosphere. LLZO pellets were prepared by pressing the as-synthesized LLZO powders via sol–gel and solid-state methods into the pellets of 12.7 mm diameter using the cold isostatic pressing (CIP) method at the pressure of 200 MPa. Pellets were further sintered at 1200 °C for 12 h in a ZrO_2 crucible covered with the same mother powders. Both sides of the LLZO pellets were coated with Ag paste and cured at 500 °C for ionic conductivity measurement.

Characterization: EIS measurements of LLZO pellets made from sol–gel and solid-state syntheses were performed using Gamry Reference 600+ with 100 mV AC amplitude and the frequency range from 1 Hz to 1 MHz. The ionic conductivity values were then calculated from the EIS datasets accordingly. XRD was performed on precursors and as-synthesized powder samples obtained at different temperatures for phase identification using Rigaku Miniflex 600 and Rigaku Ultima-III powder X-ray diffractometers with Cu Kα radiation (λ = 1.5406 Å) and scanning range from 10° to 60° with 1.2° min^{-1} scanning rate and 0.02° step size. The experimentally obtained XRD patterns were quantitatively analyzed through the Rietveld refinement. The mass fraction of each phase was determined using the reference intensity ratio (RIR) method, and the quantification was performed with the aid of the Rigaku PDXL software. TEM characterization was carried out to obtain HRTEM images as well as electron diffraction patterns using JEOL JEM-2800 TEM operated at 200 kV and Hitachi H9500 TEM operated at 300 kV. The electron beam intensity was carefully calibrated and well-controlled to avoid damage due to high-energy electron radiation.

In Situ Heating TEM: The MEMS-based heating holders (Protochips Fusion and Hitachi Blaze) were used to perform in situ heating experiments for LLZO synthesis via sol–gel and solid-state methods. For the sol–gel method, the xerogel powders were dispersed directly onto the silicon nitride member of a MEMS heating chip and then loaded into the heating holder for in situ TEM observations at various temperatures. For the solid-state method, all precursors were mixed by ball milling and pressed into a pellet, which was further cut by focused-ion beam (FIB) to make a thin solid-state precursor lamella for in situ heating experiments. The FIB sample preparation was performed using TESCAN GAIA3 SEM/FIB operated at 30 kV and finished with the 5 kV cleaning process. The in situ heating TEM experiments were conducted on a 300 kV Hitachi H9500 TEM equipped with an AMT NanoSprint5 camera (5.0 Megapixel, 40 fps) using the Hitachi Blaze holder or on a 200 kV JEOL JEM-2800 TEM equipped with a Gatan Oneview-IS camera (16 Megapixel, 25 fps) using the Protochips Fusion holder. During a typical in situ heating experiment, the temperature was increased from room temperature to an elevated temperature up to 950 °C at a constant rate of 10 °C s^{-1} and then cooled down to room temperature at the constant rate of 10 °C s^{-1}, while in some scenarios, a

variable rate ranging from 1 to 800 °C s^{-1} was applied to study the effect on the surface amorphization. The electron beam intensity was carefully controlled during imaging and blanked during the rest of heating periods to avoid electron radiation damage.

Supporting Information

Supporting Information is available from the Wiley Online Library or from the author.

Acknowledgements

This research was supported by the National Science Foundation under the CAREER Award No. 2239598. The authors acknowledge the use of facilities and instrumentation at the University of California Irvine Materials Research Institute, supported in part by the National Science Foundation Materials Research Science and Engineering Center program through the University of California Irvine Center for Complex and Active Materials (DMR-2011967). The authors also acknowledge the use of the Electron Microscopy Facility at Clemson University. The authors also thank UCI graduate students, Tom Lee and Zhaokun Wang, for their assistance in the electrochemical impedance test.

Conflict of Interest

The authors declare no conflict of interest.

Data Availability Statement

The data that support the findings of this study are available from the corresponding author upon reasonable request.

Keywords

in situ heating transmission electron microscopy (TEM), $Li_7La_3Zr_2O_{12}$ (LLZO), phase transformation, sol–gel synthesis, solid-state electrolytes, solid-state sintering, surface amorphization

Received: June 7, 2023
Revised: August 16, 2023
Published online:

[1] F. Duffner, N. Kronemeyer, J. Tübke, J. Leker, M. Winter, R. Schmuch, *Nat. Energy* **2021**, *6*, 123.
[2] Y. Li, W. Huang, Y. Li, W. Chiu, Y. Cui, *ACS Nano* **2020**, *14*, 9263.
[3] C. Wang, K. Fu, S. P. Kammampata, D. W. McOwen, A. J. Samson, L. Zhang, G. T. Hitz, A. M. Nolan, E. D. Wachsman, Y. Mo, V. Thangadurai, L. Hu, *Chem. Rev.* **2020**, *120*, 4257.
[4] J. Janek, W. G. Zeier, *Nat. Energy* **2016**, *1*, 16141.
[5] A. Manthiram, X. Yu, S. Wang, *Nat. Rev. Mater.* **2017**, *2*, 16103.
[6] J. Janek, W. G. Zeier, *Nat. Energy* **2023**, *8*, 230.
[7] Y. Li, J. T. Han, C. A. Wang, H. Xie, J. B. Goodenough, *J. Mater. Chem.* **2012**, *22*, 15357.
[8] G. Han, B. Kinzer, R. Garcia-Mendez, H. Choe, J. Wolfenstine, J. Sakamoto, *J. Eur. Ceram. Soc.* **2020**, *40*, 1999.
[9] V. Thangadurai, W. Weppner, *Adv. Funct. Mater.* **2005**, *15*, 107.
[10] V. Thangadurai, S. Narayanan, D. Pinzaru, *Chem. Soc. Rev.* **2014**, *43*, 4714.
[11] R. Murugan, V. Thangadurai, W. Weppner, *Angew. Chem., Int. Ed.* **2007**, *46*, 7778.
[12] J. Awaka, N. Kijima, H. Hayakawa, J. Akimoto, *J. Solid State Chem.* **2009**, *182*, 2046.
[13] J. Awaka, A. Takashima, K. Kataoka, N. Kijima, Y. Idemoto, J. Akimoto, *Chem. Lett.* **2010**, *40*, 60.
[14] S. Song, Y. Xu, Y. Ruan, H. Wang, D. Zhang, J. Thokchom, D. Mei, *ACS Appl. Energy Mater.* **2021**, *4*, 8517.
[15] I. Koresh, B. A. Klein, Z. Tang, V. K. Michaelis, T. Troczynski, *Solid State Ionics* **2022**, *380*, 115938.
[16] Y. Li, J. T. Han, C. A. Wang, S. C. Vogel, H. Xie, M. Xu, J. B. Goodenough, *J. Power Sources* **2012**, *209*, 278.
[17] A. J. Samson, K. Hofstetter, S. Bag, V. Thangadurai, *Energy Environ. Sci.* **2019**, *12*, 2957.
[18] R. P. Rao, W. Gu, N. Sharma, V. K. Peterson, M. Avdeev, S. Adams, *Chem. Mater.* **2015**, *27*, 2903.
[19] P. Barai, T. Fister, Y. Liang, J. Libera, M. Wolfman, X. Wang, J. Garcia, H. Iddir, V. Srinivasan, *Chem. Mater.* **2021**, *33*, 4337.
[20] E. Kazyak, K. H. Chen, K. N. Wood, A. L. Davis, T. Thompson, A. R. Bielinski, A. J. Sanchez, X. Wang, C. Wang, J. Sakamoto, N. P. Dasgupta, *Chem. Mater.* **2017**, *29*, 3785.
[21] Y. Tian, Y. Zhou, Y. Liu, C. Zhao, W. Wang, Y. Zhou, *Solid State Ionics* **2020**, *354*, 115407.
[22] H. Wang, Y.-I. I. Jang, B. Huang, D. R. Sadoway, Y. M. Chiang, *J. Electrochem. Soc.* **1999**, *146*, 473.
[23] J. Cui, H. Zheng, Z. Zhang, S. Hwang, X. Q. Yang, K. He, *Matter* **2021**, *4*, 1335.
[24] H. Zheng, X. Lu, K. He, *J. Energy Chem.* **2022**, *68*, 454.
[25] H. Park, H. Park, K. Song, S. H. Song, S. Kang, K. H. Ko, D. Eum, Y. Jeon, J. Kim, W. M. Seong, H. Kim, J. Park, K. Kang, *Nat. Chem.* **2022**, *14*, 614.
[26] C. Y. Huang, Y. T. Tseng, H. Y. Lo, J. K. Chang, W. W. Wu, *Nano Energy* **2020**, *71*, 104625.
[27] J. P. Attfield, G. Férey, *J. Solid State Chem.* **1989**, *82*, 132.
[28] J. Sastre, M. H. Futscher, L. Pompizi, A. Aribia, A. Priebe, J. Overbeck, M. Stiefel, A. N. Tiwari, Y. E. Romanyuk, *Commun. Mater.* **2021**, *2*, 76.
[29] J. S. Kim, H. Kim, M. Badding, Z. Song, K. Kim, Y. Kim, D. J. Yun, D. Lee, J. Chang, S. Kim, D. Im, S. Park, S. H. Kim, S. Heo, *J. Mater. Chem. A* **2020**, *8*, 16892.
[30] C. Wang, W. Ping, Q. Bai, H. Cui, R. Hensleigh, R. Wang, A. H. Brozena, Z. Xu, J. Dai, Y. Pei, C. Zheng, G. Pastel, J. Gao, X. Wang, H. Wang, J. C. Zhao, B. Yang, X. Rayne Zheng, J. Luo, Y. Mo, B. Dunn, L. Hu, *Science* **2020**, *368*, 521.
[31] M. Hong, Q. Dong, H. Xie, B. C. Clifford, J. Qian, X. Wang, J. Luo, L. Hu, *ACS Energy Lett.* **2021**, *6*, 3753.
[32] L. C. Hoff, W. S. Scheld, C. Vedder, J. Stollenwerk, *Proc. SPIE* **2022**, *11989*, 108.
[33] W. Sebastian Scheld, L. Charlotte Hoff, C. Vedder, J. Stollenwerk, D. Grüner, M. Rosen, S. Lobe, M. Ihrig, A. Seok, M. Finsterbusch, S. Uhlenbruck, O. Guillon, D. Fattakhova-Rohlfing, *Appl. Energy* **2023**, *345*, 121335.
[34] D. Zhang, X. Cao, D. Xu, N. Wang, C. Yu, W. Hu, X. Yan, J. Mi, B. Wen, L. Wang, L. Zhang, *Electrochim. Acta* **2018**, *259*, 100.
[35] L. D. Trong, T. T. Thao, N. N. Dinh, *Solid State Ionics* **2015**, *278*, 228.
[36] X. Tao, Y. Liu, W. Liu, G. Zhou, J. Zhao, D. Lin, C. Zu, O. Sheng, W. Zhang, H. W. Lee, Y. Cui, *Nano Lett.* **2017**, *17*, 2967.